Journal of Computational Physics **172,** 71–98 (2001)
doi:10.1006/jcph.2001.6812, available online at http://www.idealibrary.com on IDEAL®

A Boundary Condition Capturing Method for Incompressible Flame Discontinuities[1]

Duc Q. Nguyen,* Ronald P. Fedkiw,† and Myungjoo Kang*

*Department of Mathematics, University of California Los Angeles, Los Angeles, California 90095; and †Computer Science Department, Stanford University, Stanford, California 94305
E-mail: †fedkiw@cs.stanford.edu

Received June 26, 2000; revised April 5, 2001

In this paper, we propose a new numerical method for treating two-phase incompressible flow where one phase is being converted into the other, e.g., the vaporization of liquid water. We consider this numerical method in the context of treating discontinuously thin flame fronts for incompressible flow. This method was designed as an extension of the Ghost Fluid Method (1999, *J. Comput. Phys.* **152**, 457) and relies heavily on the boundary condition capturing technology developed in Liu *et al*. (2000, *J. Comput. Phys.* **154**, 15) for the variable coefficient Poisson equation and in Kang *et al*. (in press *J. Comput. Phys.*) for multiphase incompressible flow. Our new numerical method admits a sharp interface representation similar to the method proposed in Helenbrook *et al*. (1999, *J. Comput. Phys.* **148**, 366). Since the interface boundary conditions are handled in a simple and straightforward fashion, the code is very robust, e.g. no special treatment is required to treat the merging of flame fronts. The method is presented in three spatial dimensions, with numerical examples in one, two, and three spatial dimensions.

1. INTRODUCTION

Consider multiphase incompressible flow including the effects of viscosity, surface tension, and gravity. Any numerical approach to this problem needs both a method for tracking (or capturing) the interface location as well as a method for enforcing the appropriate boundary conditions at the tracked interface. See [1, 19, 23] (and [2]) for numerical methods that used front tracking, volume of fluid and level set methods, respectively, for tracking the location of the multiphase interface. All of these methods use a δ-function formulation to enforce the appropriate boundary conditions at the multiphase interface. This δ-function formulation was originally proposed as part of the "immersed boundary" method for computing

[1] Research supported in part by ONR N00014-97-1-0027.

0021-9991/01 $35.00

solutions to the incompressible Navier–Stokes equations in the presence of a submersed elastic interface; see [16, 17]. The numerical methods in [1, 2, 19, 23] all extend the δ-function formulation of [16] to treat multiphase incompressible flow.

One drawback of the δ-function formulation is that it smears out numerical quantities across the interface producing a continuous profile for the density, viscosity, and pressure. This numerical smearing can be problematic, e.g., a continuous pressure profile does not adequately model surface tension forces and [1, 2, 19, 23] need to add source terms to the right-hand side of the momentum equations in order to numerically model these forces. An alternative strategy for enforcing the interface boundary conditions is based on the Ghost Fluid Method (GFM) of [4]. In [13], the authors extended the GFM to treat the variable coefficient Poisson equation in the presence of an immersed interface. In [12], the authors used the method from [13] to devise a numerical method for multiphase incompressible flow that allows for a nonsmeared numerical representation of the density, viscosity, and pressure. Moreover, since surface tension was modeled directly with a jump in pressure across the interface, there was no need to add source terms to the right-hand side of the momentum equations as was done in [1, 2, 19, 23].

For multiphase incompressible flow, the interface moves with local fluid velocity only and individual fluid particles do not cross the interface. In this paper, we consider interfaces where a reaction is taking place and the interface moves with the local unreacted fluid velocity plus a reaction term that accounts for the conversion of one fluid into the other. That is, we account for the movement of material across the interface. Consider, for example, an interface separating liquid and gas regions where the liquid is actively vaporizing into the gaseous state. See [11] for a front tracking approach to this problem using a δ-function formulation to treat the interface boundary conditions. See [22] and [24] for level set based and volume of fluid based (respectively) approaches to this same problem also using a δ-function formulation. References [11, 22, 24] solve an equation for the temperature in order to determine the rate at which one material is converted into another.

As another example of reacting interfaces, consider combustion in premixed flames. Assuming that the flame front is infinitely thin allows one to treat the flame front as a discontinuity separating two incompressible flows. The unreacted material undergoes reaction as it crosses the interface producing a lower density (higher volume) reacted material. See [20] for a front tracking approach to this problem using a δ-function formulation. The flame speeds in [20] were determined with the aid of the G-equation [14, 25], so an extra equation for the temperature was not needed.

In the examples mentioned above, the density of the incompressible material tends to be different on different sides of the interface. The material must instantaneously expand as it crosses the interface implying that the normal velocity is discontinuous across the interface, i.e. in addition to discontinuity of the density, viscosity, and pressure. The methods in [11, 20, 22, 24] are all based on the δ-function formulation and thus smear out this velocity jump forcing a continuous velocity field across the interface. This can be quite problematic since this numerical smearing adds a compressible character to the flow field near the interface, i.e. the divergence-free condition is not exactly satisfied in each separate subdomain. In addition, difficulties arise when trying to determine the interface velocity which depends in part on the local velocity of the unreacted material. Near the interface, the velocity of the unreacted material contains large $O(1)$ numerical errors where it has been nonphysically forced to be continuous with the velocity of the reacted material. Partial solutions to these problems were proposed in [9] where the authors were able to remove the numerical smearing of the

normal velocity obtaining a sharp interface profile. Unfortunately, the interface treatment in [9] was considerably intricate and the calculation had to be terminated if two flame fronts were significantly close to each other, i.e. this method cannot handle the simple merging of flame discontinuities. On the other hand, this method was used to obtain rather impressive results in [10] for problems in which the flame fronts do not merge or become highly curved.

In this paper, we propose a new numerical method for treating two-phase incompressible flow where one phase is being converted into the other. This method was designed as an extension of the Ghost Fluid Method [4] and relies heavily on the boundary condition capturing technology developed in [13] for the variable coefficient Poisson equation and in [12] for multiphase incompressible flow. Our new numerical method admits a sharp interface representation similar to the method proposed in [9]. In addition, the interface boundary conditions are handled in a simple and straightforward fashion making the code very robust, e.g., no special treatment is required to treat the merging of flame fronts. Numerical results are presented in one, two, and three spatial dimensions.

2. EQUATIONS

2.1. Euler Equations

The basic equations for inviscid incompressible flow are

$$\rho_t + \vec{V} \cdot \nabla \rho = 0 \tag{1}$$

$$u_t + \vec{V} \cdot \nabla u + \frac{p_x}{\rho} = 0 \tag{2}$$

$$v_t + \vec{V} \cdot \nabla v + \frac{p_y}{\rho} = 0 \tag{3}$$

$$w_t + \vec{V} \cdot \nabla w + \frac{p_z}{\rho} = 0, \tag{4}$$

where t is the time, (x, y, z) are the spatial coordinates, ρ is the density, $\vec{V} = \langle u, v, w \rangle$ is the velocity field, p is the pressure, and $\nabla = \langle \frac{\partial}{\partial x}, \frac{\partial}{\partial y}, \frac{\partial}{\partial z} \rangle$. In addition, the divergence-free condition is $\nabla \cdot \vec{V} = 0$. The equations for the velocities can be written in condensed notation as a row vector

$$\vec{V} + \left(\vec{V} \cdot \nabla\right)\vec{V} + \frac{\nabla p}{\rho} = 0. \tag{5}$$

2.2. Interface Velocity

When treating multiphase incompressible flow, one needs an expression for the velocity, $\vec{W}$, of the interface. If the interface is a simple contact discontinuity, then the interface moves with the local fluid velocity only, i.e., $\vec{W} = \vec{V}$. Many numerical methods use only the normal velocity of the interface, i.e., $\vec{W} = D\vec{N}$ where D is the normal component of the interface velocity and $\vec{N} = \langle n_1, n_2, n_3 \rangle$ is the local unit normal to the interface. In the case of a contact discontinuity, $D = V_N = \vec{V} \cdot \vec{N}$.

Throughout this text, *unreacted* and *reacted* incompressible flows are separated by an interface across which the unreacted material is converted into the reacted material. The "u" and "r" subscripts are used to refer to the unreacted and reacted materials, respectively. The normal component of the interface velocity is calculated by adding the unreacted local fluid

velocity to the flame speed, S. That is, $D = (V_N)_u + S$ where $(V_N)_u$ is calculated using the velocity of the unreacted material only. This is important to note since V_N is discontinuous across the interface.

In the numerical examples, the flame speed is defined as $S = S_o + \sigma\kappa$, where S_o and σ are constants and κ is the local curvature of the interface.

2.3. Jump Conditions

Conservation of mass and momentum implies the standard Rankine–Hugoniot jump conditions across the interface

$$[\rho(V_N - D)] = 0 \tag{6}$$

$$\left[\rho(V_N - D)^2 + p\right] = 0, \tag{7}$$

where $[A] = A_r - A_u$ defines "$[\cdot]$" as the jump in a quantity across the interface. When $D \neq V_N$, the tangential velocities are continuous as well, i.e., $[V_{T_1}] = [V_{T_2}] = 0$, where T_1 and T_2 are the unit tangent vectors. This is true as long as $S \neq 0$, i.e., it is true as long as the front is not a contact discontinuity. In the case of a contact discontinuity, $S = 0$ and the tangential velocities are completely uncoupled across the interface reducing equations 6 and 7 to $[V_N] = [p] = 0$. For more details, see [5].

Denoting the mass flux in the moving reference frame (speed D) by

$$M = \rho_r((V_N)_r - D) = \rho_u((V_N)_u - D) \tag{8}$$

allows Eq. (6) to be rewritten as $[M] = 0$. Furthermore,

$$M = -\rho_u S \tag{9}$$

follows from substituting $D = (V_N)_u + S$ into Eq. (8).

Starting with $[D] = 0$,

$$\left[\frac{\rho V_N - \rho(V_N - D)}{\rho}\right] = 0 \tag{10}$$

$$\left[\frac{\rho V_N - M}{\rho}\right] = 0 \tag{11}$$

and

$$[V_N] = M\left[\frac{1}{\rho}\right], \tag{12}$$

where the last equation follows since $[M] = 0$. It is more convenient to write

$$[\vec{V}] = M\left[\frac{1}{\rho}\right]\vec{N} \tag{13}$$

as a summary of Eq. (12) and $[V_{T_1}] = [V_{T_2}] = 0$. Taking the dot product of Eq. (13) and $\vec{N}$ results in Eq. (12), while taking the dot product of Eq. (13) and $\vec{T}_1$ or $\vec{T}_2$, results in $[V_{T_1}] = 0$ and $[V_{T_2}] = 0$, respectively.

Equation (7) can be rewritten as

$$\left[\frac{M^2}{\rho} + p\right] = 0 \tag{14}$$

or as

$$[p] = -M^2 \left[\frac{1}{\rho}\right] \tag{15}$$

again using $[M] = 0$.

2.4. Level Set Equation

The level set equation

$$\phi_t + \vec{W} \cdot \nabla\phi = 0 \tag{16}$$

is used to keep track of the interface location as the set of points where $\phi = 0$. The unreacted and reacted materials are then designated by the points where $\phi > 0$ and $\phi \leq 0$, respectively. Using $\phi \leq 0$ instead of $\phi = 0$ for the reacted points removes the measure zero ambiguity of points that happen to lie on the interface. In this sense, the numerical interface lies in between $\phi = 0$ and the positive values of ϕ and can be located numerically by finding the zero level of ϕ. To keep the values of ϕ close to those of a signed distance function, i.e., $|\nabla\phi| = 1$, the reinitialization equation

$$\phi_\tau + S(\phi_o)(|\nabla\phi| - 1) = 0 \tag{17}$$

is iterated for a few steps in ficticious time, τ. The level set function is used to compute the normal

$$\vec{N} = \frac{\nabla\phi}{|\nabla\phi|} \tag{18}$$

and the curvature

$$\kappa = -\nabla \cdot \vec{N} \tag{19}$$

in a standard fashion. For more details on the level set function, see [4, 12, 15, 19].

3. NUMERICAL METHOD

A standard MAC grid is used for discretization, where $p_{i,j,k}$, $\rho_{i,j,k}$ and $\phi_{i,j,k}$ exist at the cell centers (grid points) and $u_{i\pm1/2,j,k}$, $v_{i,j\pm1/2,k}$, and $w_{i,j,k\pm1/2}$ exist at the appropriate cell walls. See [7] and [18] for more details.

3.1. Extending the Velocity Field

Since the normal velocity is discontinuous across the interface, one has to use caution when applying numerical discretizations near the interface. For example, when discretizing the unreacted fluid velocity near the interface, one should avoid using values of the reacted fluid velocity. Following the Ghost Fluid Methodology in [4], a band of ghost cells on the reacted side of the interface is populated with unreacted ghost velocities that can be used in the discretization of the unreacted fluid velocity. Similarly, reacted ghost velocities are defined on a band of ghost cells on the unreacted side of the interface and used in the discretization of the reacted fluid velocity.

The term ϕ is defined at the grid nodes, and its values on the offset MAC grid are computed with simple averaging, e.g., $\phi_{i+1/2,j,k} = \frac{\phi_{i,j,k} + \phi_{i+1,j,k}}{2}$. The MAC grid values of ϕ can then be used to determine which values of the velocity field correspond to unreacted material and which correspond to reacted material. At each MAC grid location that corresponds to a reacted fluid velocity, the jump conditions in Eq. (13) are used to define a new unreacted ghost velocity according to

$$u_u^G = u_r - M\left(\frac{1}{\rho_r} - \frac{1}{\rho_u}\right)n_1 \tag{20}$$

$$v_u^G = v_r - M\left(\frac{1}{\rho_r} - \frac{1}{\rho_u}\right)n_2 \tag{21}$$

and

$$w_u^G = w_r - M\left(\frac{1}{\rho_r} - \frac{1}{\rho_u}\right)n_3, \tag{22}$$

where n_1, n_2, and n_3 are computed at the appropriate MAC grid locations using simple averaging, e.g., $(n_1)_{i+1/2,j,k} = \frac{(n_1)_{i,j,k} + (n_1)_{i+1,j,k}}{2}$. Similarly, reacted ghost velocities are calculated at unreacted MAC grid locations using

$$u_r^G = u_u + M\left(\frac{1}{\rho_r} - \frac{1}{\rho_u}\right)n_1 \tag{23}$$

$$v_r^G = v_u + M\left(\frac{1}{\rho_r} - \frac{1}{\rho_u}\right)n_2 \tag{24}$$

and

$$w_r^G = w_u + M\left(\frac{1}{\rho_r} - \frac{1}{\rho_u}\right)n_3. \tag{25}$$

3.2. Level Set Equation

The level set function is evolved in time from ϕ^n to ϕ^{n+1} using nodal velocities, $\vec{W} = D\vec{N}$, where $\vec{N}$ is computed at each grid node using Eq. (18) as described in [12]. In general, $D = (V_N)_u + S$ where $(V_N)_u$ is the normal velocity of the unreacted material and $S = S_o + \sigma\kappa$ is the flame speed. If S depends on the local curvature of the front, i.e., $\sigma \neq 0$, then $\vec{W}$ is split into a purely convective component $\vec{W}_c = ((V_N)_u + S_o)\vec{N}$ and a curvature component $\sigma\kappa\vec{N}$ so that Eq. (16) can be rewritten as

$$\phi_t + \vec{W}_c \cdot \nabla\phi = -\sigma\kappa|\nabla\phi|, \tag{26}$$

with the curvature term isolated on the right-hand side. Then κ is discretized according to Eq. (19) as discussed in [12], and $|\nabla\phi|$ is discretized with standard central differencing. It is interesting to note that an alternate definition of $\vec{W}_c = \vec{V}_u + S_o\vec{N}$ can be used in Eq. (26) as well. Both of the two nonequivalent definitions of $\vec{W}_c$ give the same result in the dot product $\vec{W}_c \cdot \nabla\phi$ since they only differ in the direction tangential to $\nabla\phi$.

The normal velocity of the unreacted material, $(V_N)_u$, is needed in a band about the front so that Eq. (26) can be solved locally to update the interface location. The nodal values of the unreacted velocity, $\vec{V}_u$, are determined using simple averaging of the MAC

grid values making use of the appropriate ghost values (defined above) where needed, i.e., $u_{i,j,k} = \frac{u_{i-1/2,j,k} + u_{i+1/2,j,k}}{2}$, $v_{i,j,k} = \frac{v_{i,j-1/2,k} + v_{i,j+1/2,k}}{2}$, and $w_{i,j,k} = \frac{w_{i,j,k-1/2} + w_{i,j,k+1/2}}{2}$ are used to calculate the nodal values of the unreacted velocity. Then $(V_N)_u = \vec{V}_u \cdot \vec{N}$ is used to define the unreacted normal velocity at each grid node.

Detailed discretizations for the convective part of Eq. (26), i.e., $\vec{W}_c \cdot \nabla\phi$, and for Eq. (17) are given in [4]. Note that the fifth-order WENO discretization from [4] is used to discretize the convective part of Eq. (26) and the spatial terms in Eq. (17) for the numerical examples in this paper.

3.3. Projection Method

First, $\vec{V}^* = \langle u^*, v^*, w^* \rangle$ is defined by

$$\frac{\vec{V}^* - \vec{V}^n}{\Delta t} + (\vec{V} \cdot \nabla)\vec{V} = 0, \tag{27}$$

and then the velocity field at the new time step, $\vec{V}^{n+1} = \langle u^{n+1}, v^{n+1}, w^{n+1} \rangle$, is defined by

$$\frac{\vec{V}^{n+1} - \vec{V}^*}{\Delta t} + \frac{\nabla p}{\rho} = 0, \tag{28}$$

so that combining Eqs. 27 and 28 to eliminate $\vec{V}^*$ results in Eq. (5). Taking the divergence of Eq. (28) gives

$$\nabla \cdot \left(\frac{\nabla p}{\rho} \right) = \frac{\nabla \cdot \vec{V}^*}{\Delta t} \tag{29}$$

after setting $\nabla \cdot \vec{V}^{n+1}$ to zero. Equations (28) and (29) can be rewritten as

$$\vec{V}^{n+1} - \vec{V}^* + \frac{\nabla p^*}{\rho} = 0 \tag{30}$$

and

$$\nabla \cdot \left(\frac{\nabla p^*}{\rho} \right) = \nabla \cdot \vec{V}^* \tag{31}$$

eliminating their dependence on Δt by using a scaled pressure, $p^* = p\Delta t$. See [3, 7, 18] for more details.

3.4. Convection Terms

The MAC grid stores u values at $\vec{x}_{i\pm1/2,j,k}$. Updating $u^*_{i\pm1/2,j,k}$ in Eq. (27) requires the discretization of $\vec{V} \cdot \nabla u$ at $\vec{x}_{i\pm1/2,j,k}$. First, simple averaging can be used to define $\vec{V}$ at $\vec{x}_{i\pm1/2,j,k}$, i.e.,

$$v_{i+\frac{1}{2},j,k} = \frac{v_{i,j-\frac{1}{2},k} + v_{i,j+\frac{1}{2},k} + v_{i+1,j-\frac{1}{2},k} + v_{i+1,j+\frac{1}{2},k}}{4} \tag{32}$$

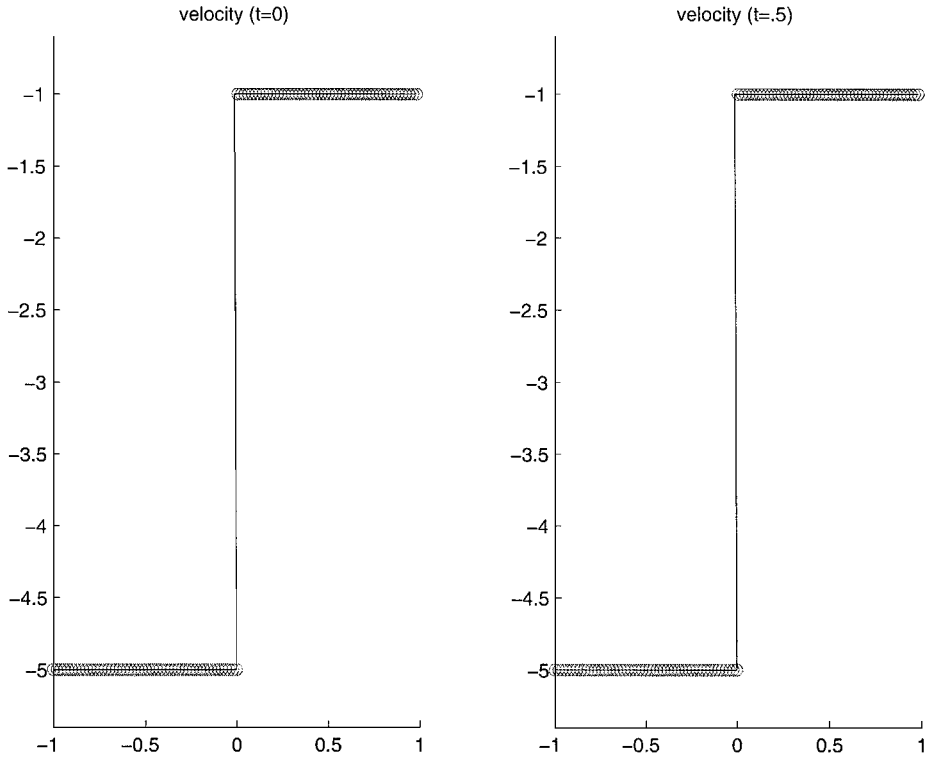

FIG. 1. Stationary flame.

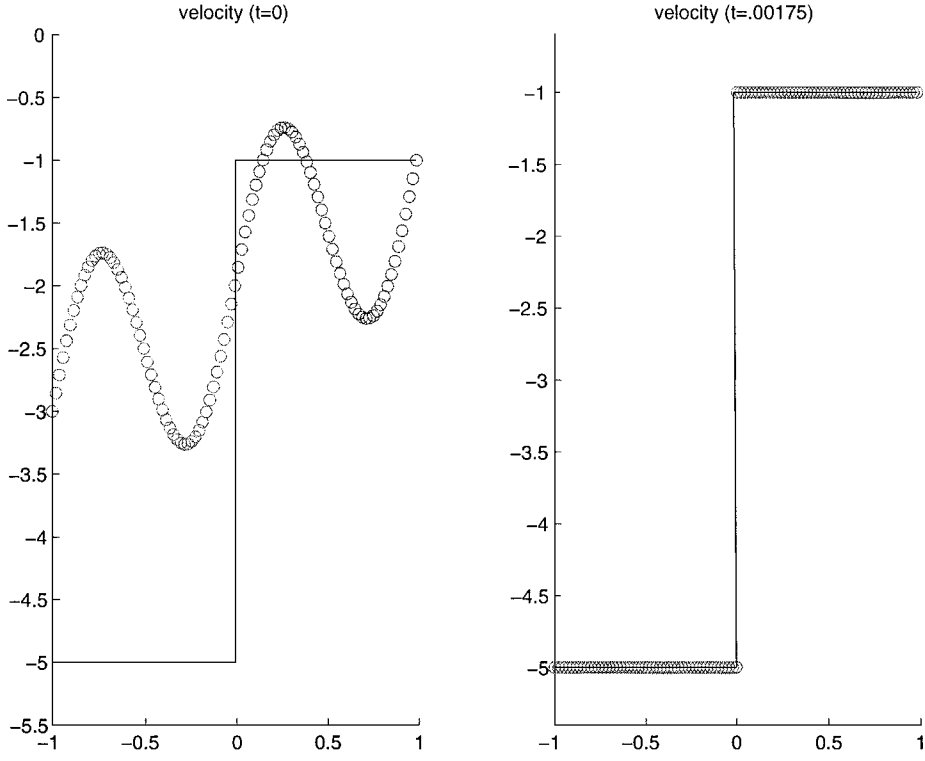

FIG. 2. Stationary flame with a poor choice of initial data.

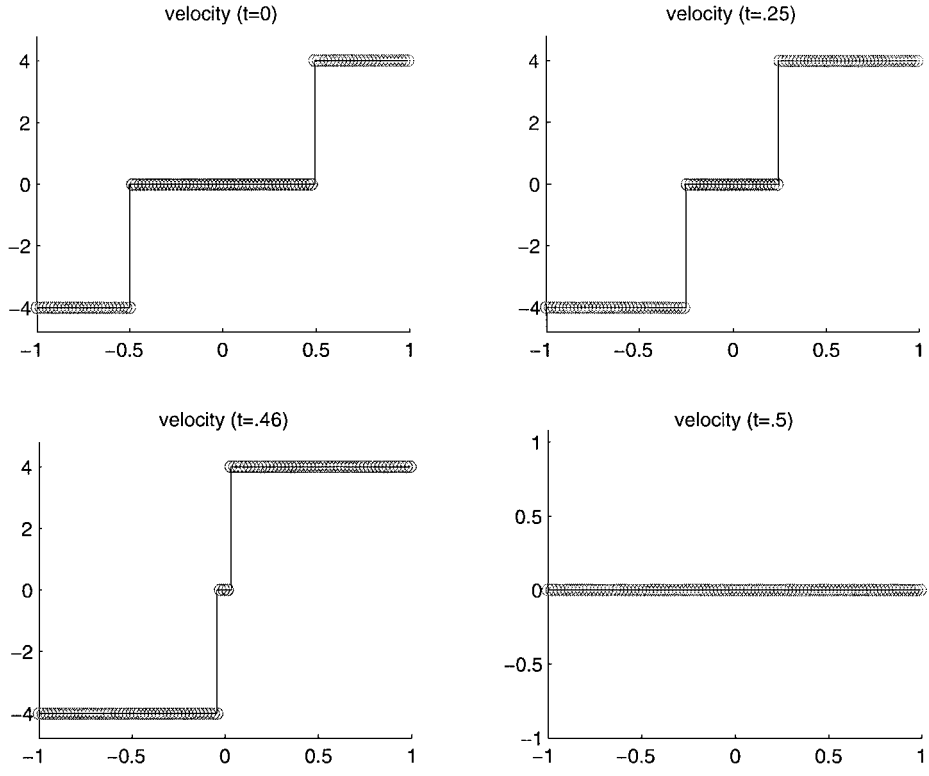

FIG. 3. Merging flames.

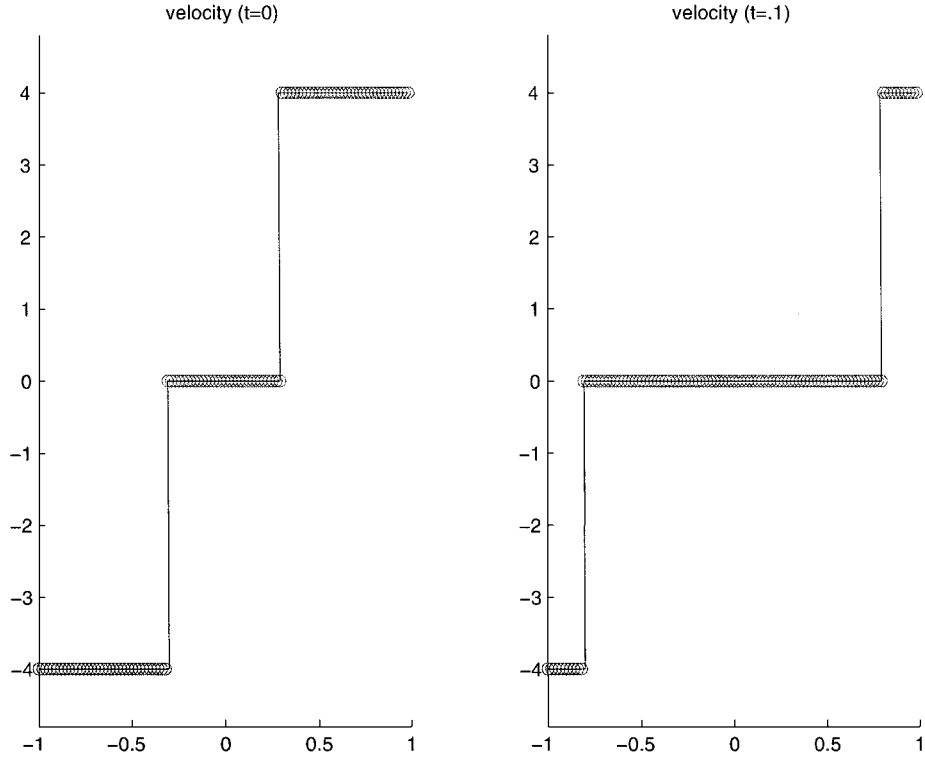

FIG. 4. Separating flames.

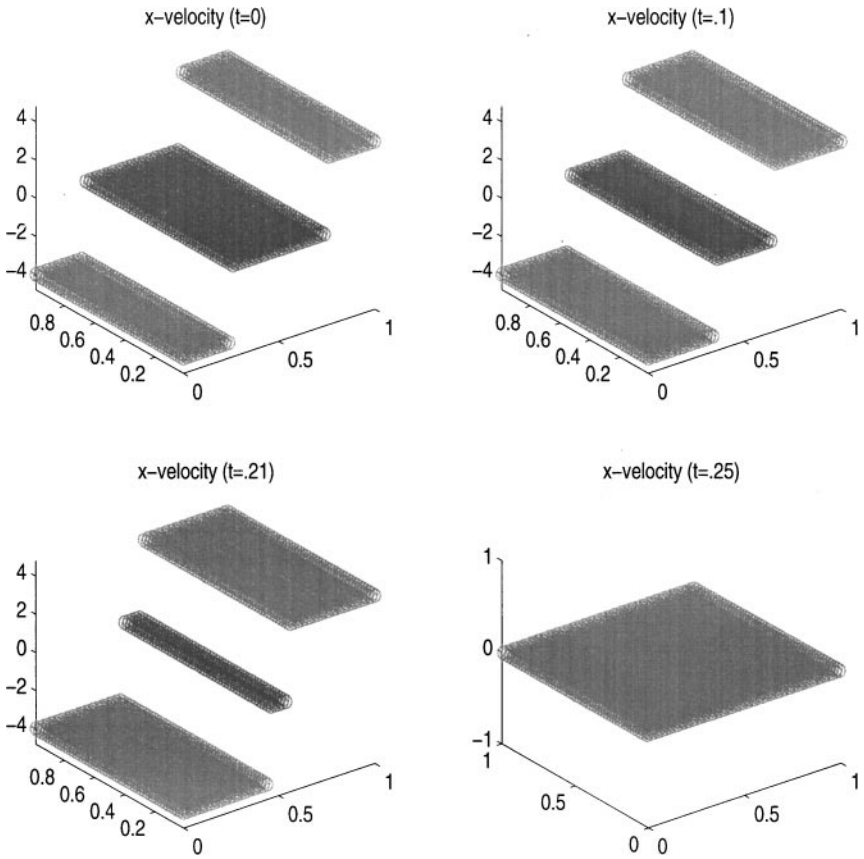

FIG. 5. Merging planar flames in two spatial dimensions.

and

$$w_{i+\frac{1}{2},j,k} = \frac{w_{i,j,k-\frac{1}{2}} + w_{i,j,k+\frac{1}{2}} + w_{i+1,j,k-\frac{1}{2}} + w_{i+1,j,k+\frac{1}{2}}}{4} \tag{33}$$

define v and w at $\vec{x}_{i+1/2,j,k}$ while $\mathbf{u}$ is already defined there. Then the $\vec{V} \cdot \nabla u$ term on the offset $\vec{x}_{i\pm1/2,j,k}$ grid can be discretized in the same fashion as the $\vec{V} \cdot \nabla \phi$ term on the regular $\vec{x}_{i,j,k}$ grid using the method outlined in [4] for Eq. (16). The terms $v^*_{i,j\pm1/2,k}$ and $w^*_{i,j,k\pm1/2}$ are updated in a similar manner. For more details, see [12]. Note that the third-order ENO discretization from [4] is used in the examples section.

It is important to note that the ghost values of the extended velocity field are used in this discretization of $\vec{V}^*$. That is, unreacted fluid velocities are discretized with the aid of the unreacted ghost velocities avoiding the use of any reacted velocities that would pollute the solution. Similarly, the reacted fluid velocities are discretized using their ghost values avoiding the unreacted fluid velocities in the discretization.

Once again, using the GFM philosophy [4], values for $\vec{V}^*_u$ and $\vec{V}^*_r$ are determined on the appropriate side of the interface *and* on a band including the interface. For example, $\vec{V}^*_u$ is computed on both the unreacted side of the interface and on a band of ghost cells on the reacted side of the interface. This is done to alleviate problems that occur when the interface moves through the grid, changing the character of the solution from unreacted to reacted or

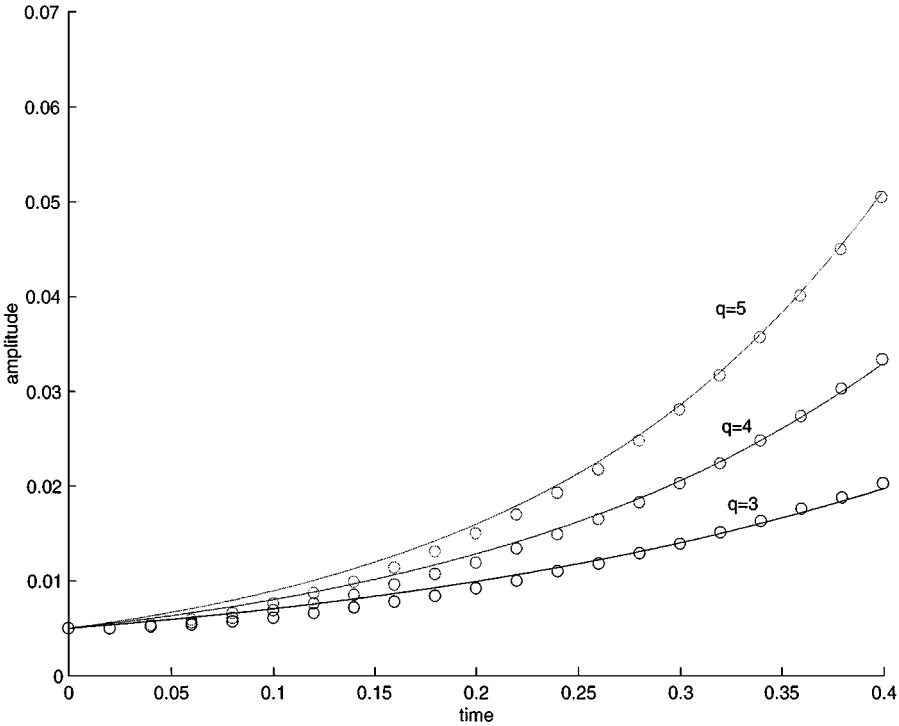

FIG. 6. Darrieus–Landau instability—exponential growth of the amplitude.

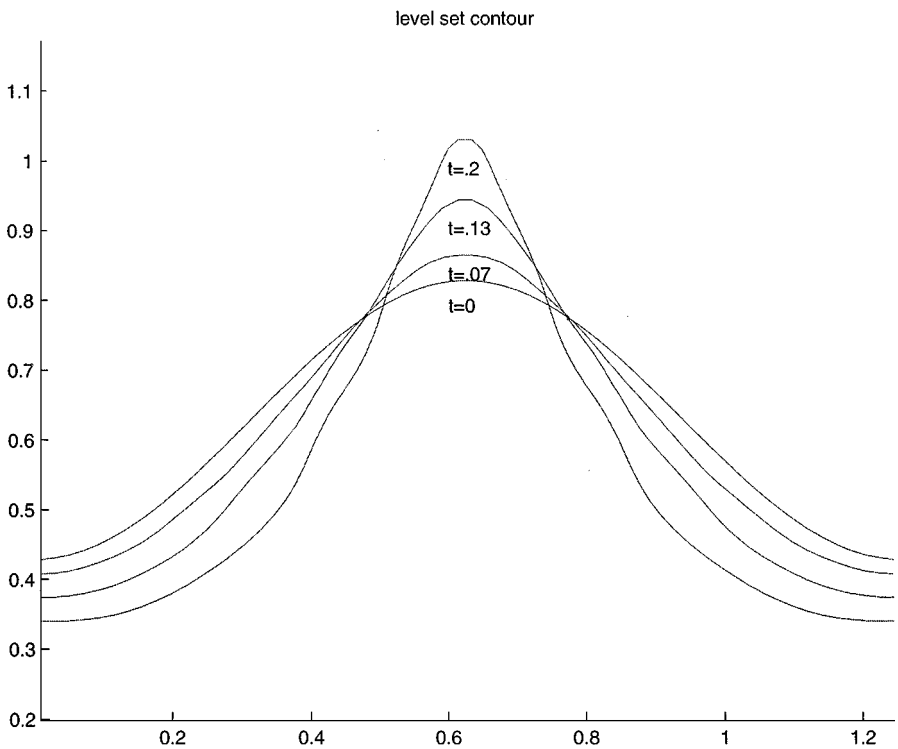

FIG. 7. Large amplitude perturbation—time evolution.

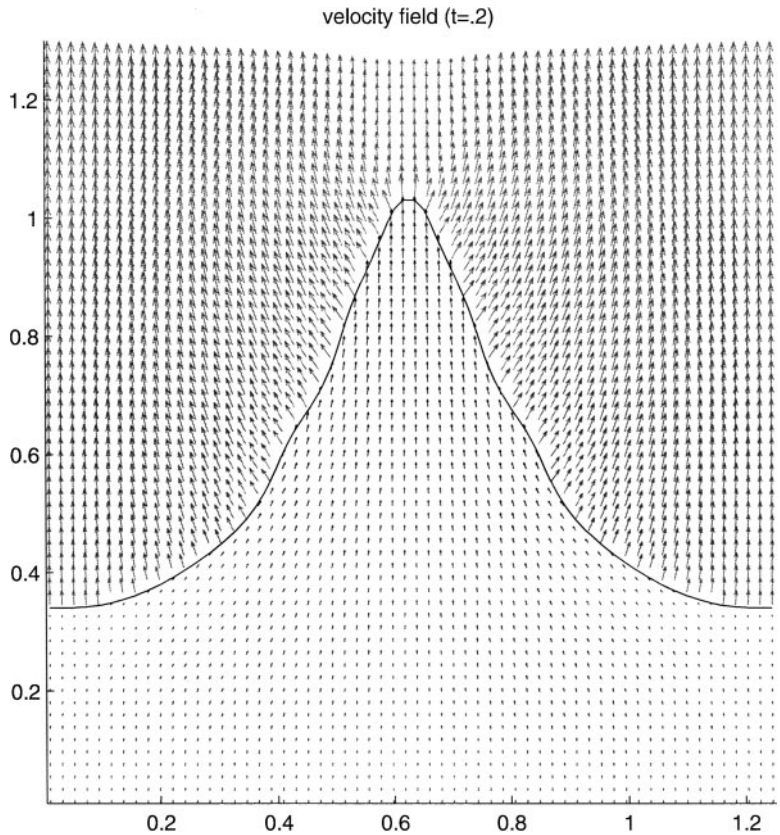

FIG. 8. Large amplitude perturbation—converging to diverging velocity field with a discontinuous normal velocity across the interface.

vice versa. As the interface moves, as dictated by the evolution of ϕ^n to ϕ^{n+1}, one always has appropriate values for $\vec{V}_u^*$ and $\vec{V}_r^*$ where needed.

3.5. Poisson Equation

Once $\vec{V}^*$ has been updated with Eq. (27), the right-hand side of Eq. (31) is discretized using standard central differencing, e.g.,

$$(u_x^*)_{i,j,k} = \frac{u^*_{i+\frac{1}{2},j,k} - u^*_{i-\frac{1}{2},j,k}}{\Delta x} \tag{34}$$

is used to compute u_x^*. Once again, the ghost values of the extended velocity fields are used to compute these derivatives so that unreacted and reacted velocities are not incorrectly mixed. Then the techniques presented in [13] for the variable coefficient Poisson equation are used to solve Eq. (31) for the pressure at the grid nodes. The resulting pressure is used to find $\vec{V}^{n+1}$ in Eq. (30), taking care to compute the derivatives of the pressure in *exactly* the same way as they were computed in Eq. (31) using the techniques in [13].

The techniques in [13] require a level set function to describe the interface location. We use ϕ^{n+1} as opposed to ϕ^n, since we wish to find the pressure that will make $\vec{V}^{n+1}$ divergence-free in Eq. (30). This implies that both Eqs. (30) and (31) should use $\rho^{n+1} = \rho(\phi^{n+1})$ when deciding whether to use ρ_u or ρ_r at a specific grid point.

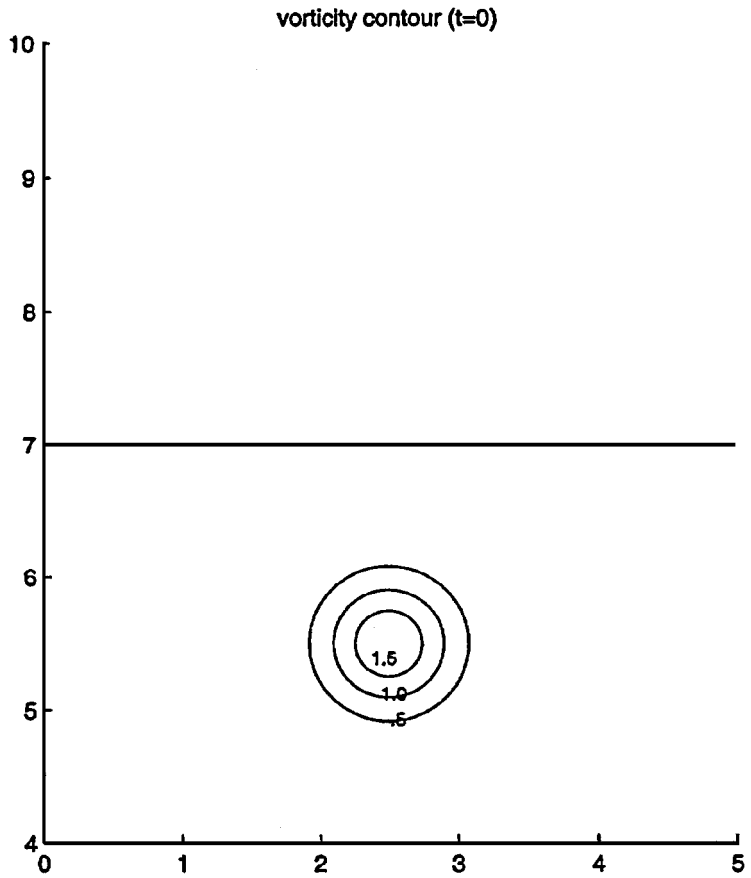

FIG. 9. Flame vortex interaction—initial flame and vortex locations.

Note that one can set $[\frac{p_x}{\rho}] = [\frac{p_y}{\rho}] = [\frac{p_z}{\rho}] = 0$ when solving the Poisson equation using the method in [13]. Since the full Eqs. (2), (3), and (4) are continuous across the interface, one can take the divergence of the full equations without considering jump conditions. On the other hand, the jump in pressure defined in equation 15 needs to be accounted for when solving the Poisson equation with the method in [13]. Equation 15 is rewritten as

$$[p^*] = -\Delta t M^2 \left(\frac{1}{\rho_r} - \frac{1}{\rho_u} \right) \tag{35}$$

for use Eq. (31). The $[p^*]$ is computed at each grid node.

After discretizing the Poisson equation for the pressure, the resulting system of linear equations is solved with a preconditioned conjugate gradient (PCG) method using an incomplete Choleski preconditioner [6]. The PCG algorithm is applied once for every Euler time step, or a total of three times for a third-order Runge–Kutta cycle.

3.6. Runge–Kutta

Since both second- and third-order TVD Runge–Kutta schemes [21] can be written as a convex combination of simple Euler steps, see [12, 21], it is straightforward to generalize the first-order time discretization discussed so far to third-order TVD Runge–Kutta. One

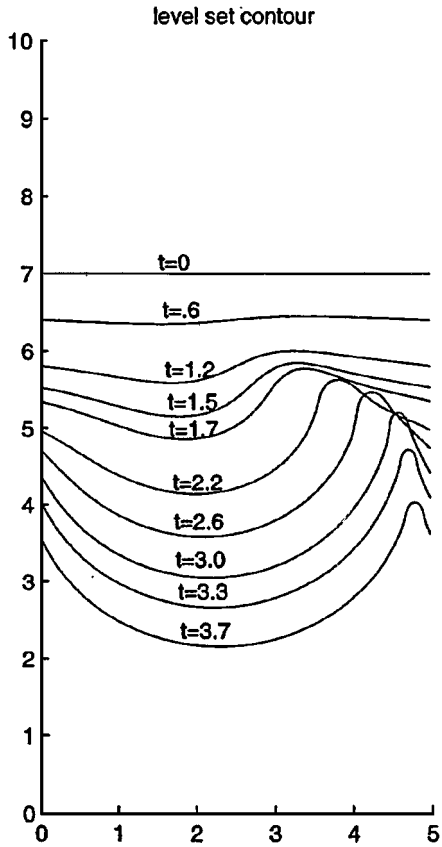

FIG. 10. Flame vortex interaction—time evolution.

difficulty in implementing Runge–Kutta methods in problems with interfaces arises when nodal values change character as the interface moves (e.g., one may inadvertently average unreacted and reacted velocity values). However, the use of the Ghost Fluid Method circumvents this difficulty.

While the values of the level set can be averaged directly, one has to be careful when averaging the velocity field in order to ensure that unreacted and reacted velocities are not accidently averaged together. Initially, $\vec{V}_u$ is defined on one side of the interface and $\vec{V}_r$ is defined on the other. Each of these velocity fields can be extended to a band about the interface using the appropriate jump conditions as outlined above. It is straightforward to use Eq. (27) to obtain $\vec{V}_u^*$ and $\vec{V}_r^*$ in the appropriate locations including a band about the interface. However, solving Eq. (28) for $\vec{V}_u^{n+1}$ and $\vec{V}_r^{n+1}$ only gives updated velocity values on the appropriate side of the interface and does not give valid values for $\vec{V}_u^{n+1}$ and $\vec{V}_r^{n+1}$ on a band including the interface. If the time n values and time $n+1$ values represent different Runge–Kutta stages, they cannot be averaged unless the time $n+1$ values are extended to include a band about the interface. Luckily, we can easily extend these values to a band about the interface using our standard velocity extension procedure outlined above. The point is that one should apply Runge–Kutta averaging to the extended velocity fields in order to avoid unwanted errors that can result from mixing the unreacted and reacted velocity fields.

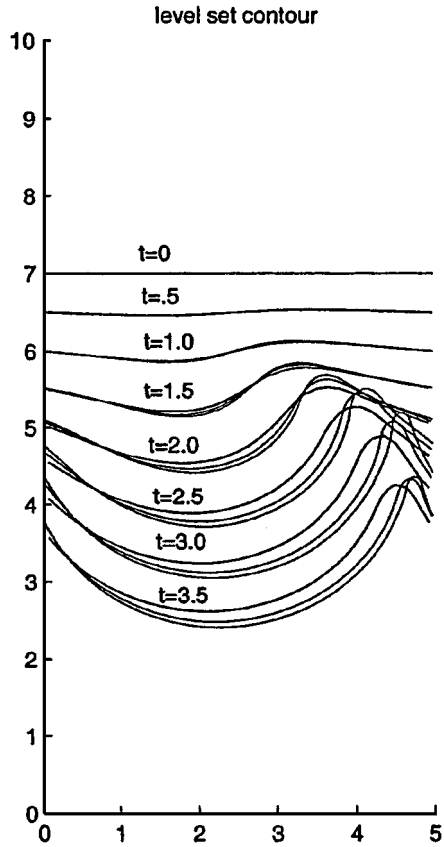

FIG. 11. Flame vortex interaction—grid refinement.

3.7. Adaptive Time Stepping

Adaptive time stepping is used where the overall time step is chosen as the minimum of the incompressible time step and the level set time step, i.e.,

$$\Delta t = .5 \min(\Delta t^I, \Delta t^L) \tag{36}$$

where we have chosen a CFL restriction of 0.5. For incompressible flow, the convective time step restriction

$$\Delta t^I \left(\frac{|u|}{\Delta x} + \frac{|v|}{\Delta y} + \frac{|w|}{\Delta z} \right) \leq 1 \tag{37}$$

needs to be satisfied at every grid point. For the level set equation, i.e., Eq. (26), the convective time step restriction

$$\Delta t^L (C_{cfl} + K_{cfl}) \leq 1 \tag{38}$$

needs to be satisfied at every grid point where

$$C_{cfl} = \frac{|w_1|}{\Delta x} + \frac{|w_2|}{\Delta y} + \frac{|w_3|}{\Delta z}, \tag{39}$$

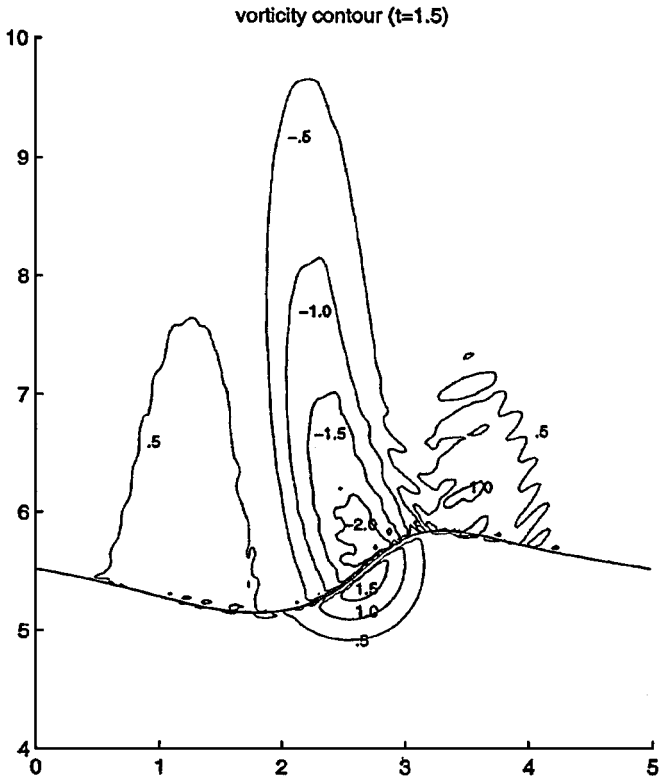

FIG. 12. Flame vortex interaction—secondary vorticity generation.

with $\vec{W}_c = \langle w_1, w_2, w_3 \rangle$ is for the convection terms and

$$K_{cfl} = \sigma \left(\frac{2}{(\Delta x)^2} + \frac{2}{(\Delta y)^2} + \frac{2}{(\Delta z)^2} \right) \tag{40}$$

is for the curvature terms.

4. EXAMPLES

In the one-dimensional examples, the Conjugate Gradient method is used without the incomplete Choleski preconditioner, since the incomplete Choleski factorization does not work in the one-dimensional case. All of the two dimensional examples utilize the PCG method with the incomplete Choleski preconditioner. Unless otherwise specified, the unreacted and reacted densities are $\rho_u = 1$ and $\rho_r = 0.2$, respectively.

4.1. One Spatial Dimension

All of the one dimensional examples are computed with 100 grid points on a $[-1, 1]$ domain. Exact solutions are shown as solid lines in the figures.

4.1.1. *Example 1*

Consider a flame with speed $S = 1$ initially located at $x = 0$. The unreacted gas flows in from the right with a velocity of $u = -1$. A Dirichlet, $p = 0$, boundary condition is

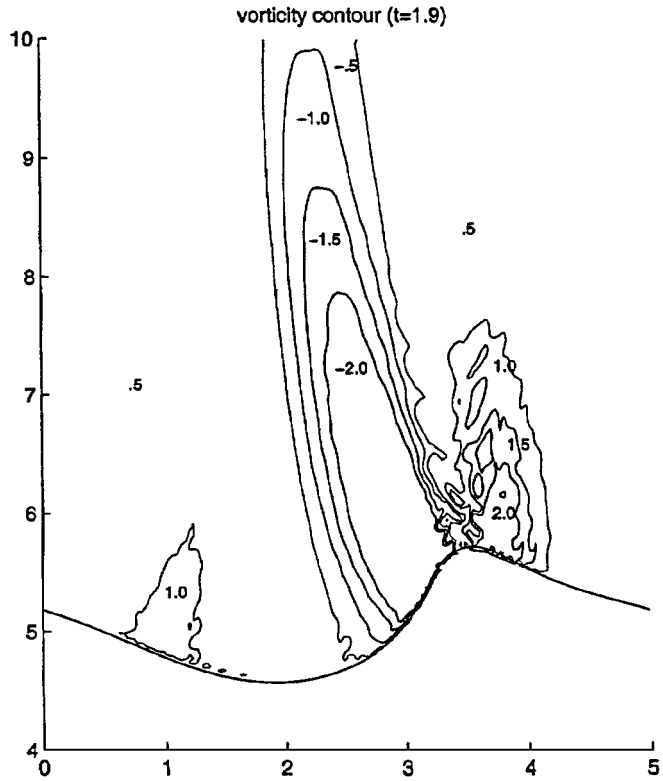

FIG. 13. Flame vortex interaction—secondary vorticity generation; 140 by 280 grid.

specified on the left-hand side of the domain, and a Neumann pressure boundary condition is used on the right-hand side of the domain to keep the inflow velocity fixed. Figure 1 shows the computed solution for this stationary flame. The calculation for Fig. 1 may seem rather trivial, since the initial data is already the exact solution. In Fig. 2, the same calculation is carried out starting with erroneous initial data. Even with this poor initial guess, the correct solution is still obtained.

4.1.2. *Example 2*

Consider two flames both with speed $S = 1$ initially located at $x = -0.5$ and $x = 0.5$. The unreacted material is at rest in the center of the domain. Dirichlet, $p = 0$, boundary conditions are specified at both ends of the domain. Initially, the reacted velocities on the left- and right-hand sides of the domain were specified as $u = -4$ and $u = 4$, respectively. Figure 3 shows the computed velocity, and illustrates the ability of our algorithm to treat merging in one dimension. After merging, the domain contains a single-phase incompressible fluid which must have a constant velocity. In the case of compressible flow, a finite speed of propagation rarefaction wave would lower the velocity to the average of the two reacted velocities (zero in this case). For incompressible flow, the "rarefaction wave" moves at infinite speed and the velocity drops to zero in one time step as shown in Fig. 3.

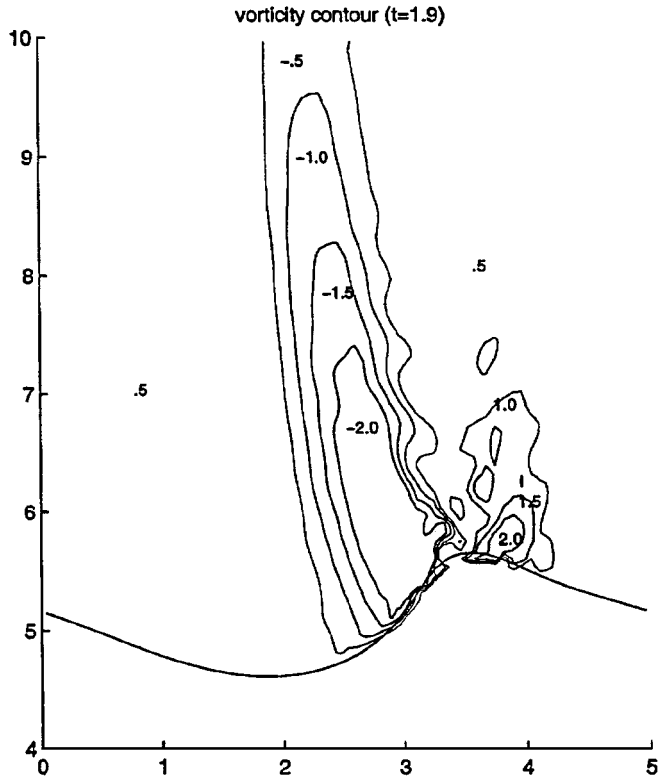

FIG. 14. Flame vortex interaction—secondary vorticity generation; 70 by 140 grid.

4.1.3. *Example 3*

Consider two flames both with speed $S = 1$ initially located at $x = -0.5$ and $x = 0.5$. The reacted material is at rest in the center of the domain and the unreacted material is flowing in with speed $|u| = 4$ from both boundaries. Dirichlet, $p = 0$, boundary conditions are specified at both ends of the domain. Figure 4 shows the computed solution as the flame front travels outward.

4.2. Two Spatial Dimensions

4.2.1. *Example 4*

Consider two planar flames both with speed $S = 1$ initially located at $x = 0.25$ and $x = 0.75$ in a $[0, 1] \times [0, 1]$ domain with the unreacted material at rest in the center of the domain. Dirichlet, $p = 0$, boundary conditions were used on the right- and left-hand sides of the domain, i.e., in the x-direction, and periodic boundary conditions were used in the y-direction. Initially, the reacted velocities on the left- and right-hand sides of the domain were specified as $\vec{V} = \langle -4, 0 \rangle$ and $\vec{V} = \langle 4, 0 \rangle$, respectively. This example is the two-dimensional equivalent of Example 2 above and illustrates the merging of two planar flames in two spatial dimensions. Results for the x-component of the velocity field are shown in Fig. 5 using a computational mesh with 50 grid cells in each direction.

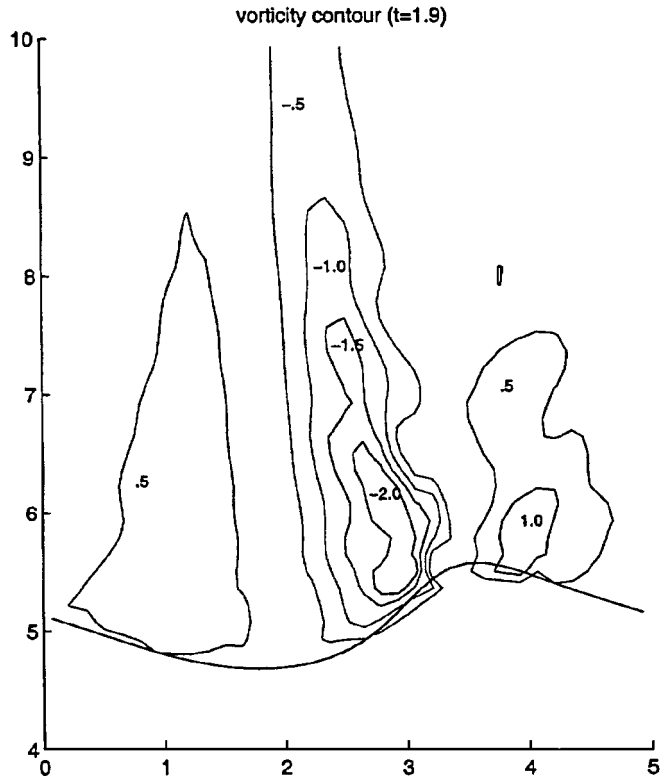

FIG. 15. Flame vortex interaction—secondary vorticity generation; 35 by 70 grid.

4.2.2. *Example 5*

In this example we consider the Darrieus–Landau instability with $S = 1$ in a $[0, \frac{2\pi}{5}] \times [0, \frac{2\pi}{5}]$ domain with 60 grid cells in each direction. The initial flame profile is a small amplitude cosine wave defined by $y = 0.005\cos(5x) + \frac{\pi}{5}$. The unreacted material is flowing in from the bottom of the domain with an initial velocity of $\vec{V} = \langle 0, 1\rangle$ and the reacted material flowing out of the top of the domain with an initial velocity of $\vec{V} = \langle 0, 5\rangle$. Dirichlet, $p = 0$, boundary conditions were used in the y-direction, and periodic boundary conditions were used in the x-direction. The initial values of $|\phi|$ were determined by placing 10,000 points (equally spaced in the x-direction) on the flame front and computing the minimum distance from this set of points to each Cartesian grid location where the values of the level set are stored. The sign of ϕ was calculated by comparing each Cartesian grid location to $y = 0.005\cos(5x) + \frac{\pi}{5}$.

The Darrieus–Landau instability results in exponential growth of the amplitude of the flame, $A(t) = A_o \exp(\omega t)$, where

$$\omega = \frac{k|M|}{\rho_u + \rho_r}\left(\sqrt{1 + \frac{\rho_u}{\rho_r} - \frac{\rho_r}{\rho_u}} - 1\right) \tag{41}$$

is the rate of exponential growth, e.g. see [9]. Figure 6 shows a plot of amplitude versus time (labeled $q = 5$ where $q = \frac{\rho_u}{\rho_b}$) as compared to the exact solution. Initially there is some disagreement, since we did not start out with the exact Darrieus–Landau velocity field, but

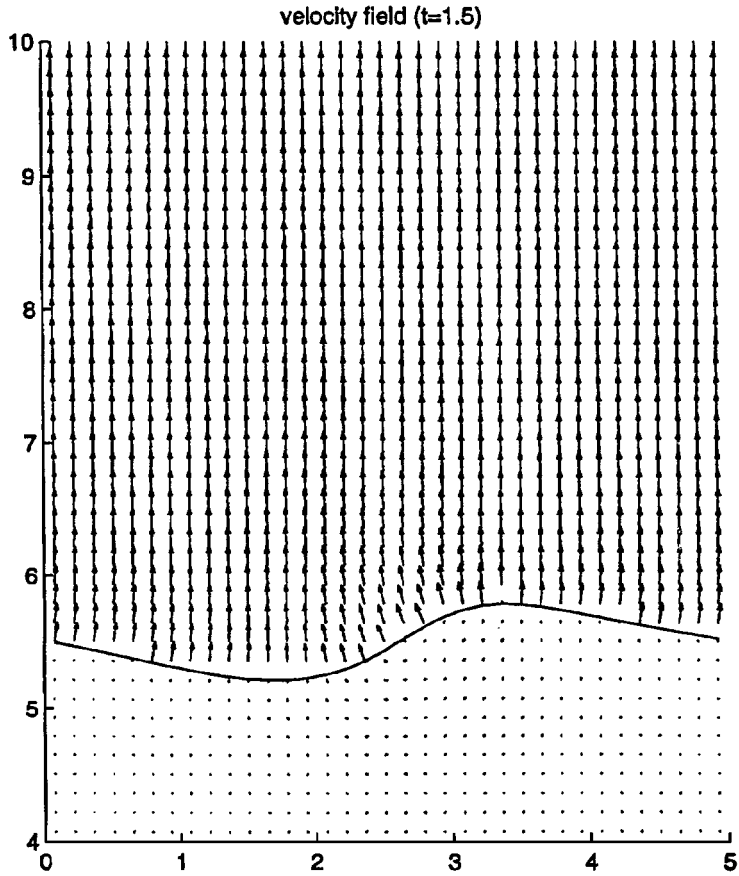

FIG. 16. Flame vortex interaction—velocity field.

instead used a piecewise constant approximation based on a planar flame profile as outlined above. Others have noticed this same initial transient when using a planar approximation for the initial velocity field [8]. Figure 6 shows the results with $\rho_r = \frac{1}{4}$ (labeled $q = 4$) and $\rho_r = \frac{1}{3}$ (labeled $q = 3$), respectively. Note that the initial outflow velocity was changed to $\vec{V} = \langle 0, 4 \rangle$ for the $q = 4$ case and to $\vec{V} = \langle 0, 3 \rangle$ for the $q = 3$ case.

Figure 7 shows the time evolution of the flame front for a large amplitude perturbation defined by $y = 0.2\cos(5x) + \frac{\pi}{5}$ for the $q = 5$ case. The velocity field at the final time of $t = 0.2$ seconds is shown in Fig. 8. The gas flow converges toward the cusp and diverges away from the cusp, and the normal component of the velocity field is appropriately discontinuous. Note that the completely continuous velocity field shown in Fig. 6 of [20] damps out the severity of the converging to diverging nature of the velocity field as it crosses the interface near the cusp.

4.2.3. *Example 6*

Consider a planar flame located at $y = 7$ in a $[0, 5] \times [0, 10]$ domain. The unreacted material is below $y = 7$ and is initially at rest while the reacted material is flowing out of the top of the domain with an initial velocity of $\vec{V} = \langle 0, 4 \rangle$. Dirichlet, $p = 0$, boundary conditions were used on the top of the domain and fixed velocity Neumann boundary

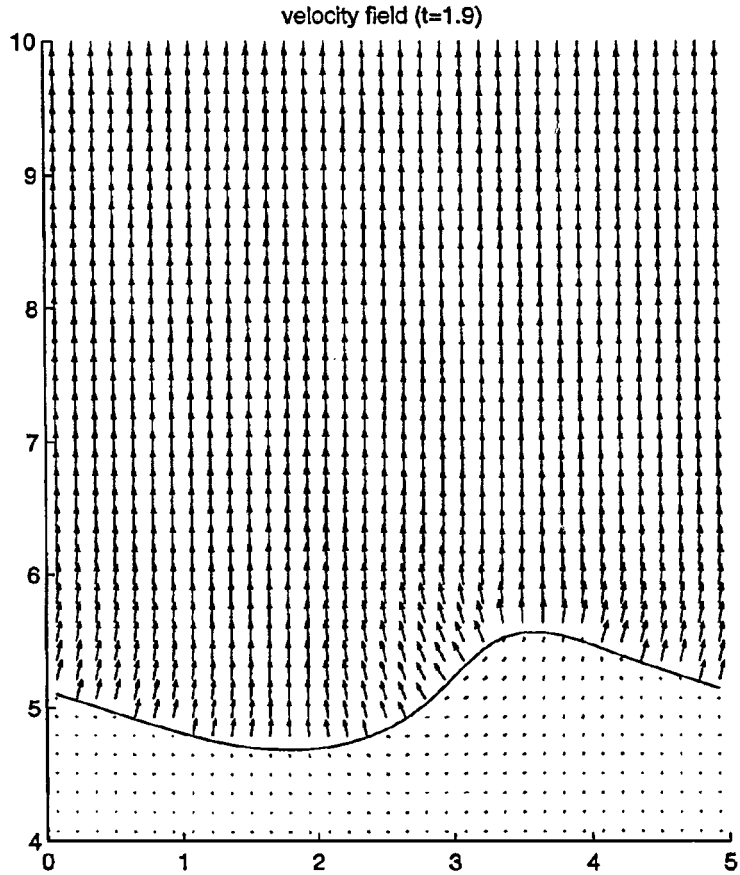

FIG. 17. Flame vortex interaction—velocity field.

conditions were used on the bottom of the domain. Periodic boundary conditions were used in the x-direction. To suppress the hydrodynamic instability development at short wavelengths, a curvature term was added to the flame speed to obtain $S = 1 + .1\kappa$.

In order to simulate flame vortex interaction, an infinite array of Oseen vortices were added to the unreacted material centered at spatial locations of $(x, y) = (2.5 + 5k, 5.5)$, where k is an integer. This adds only one vortex to the computational domain at $(x, y) = (2.5, 5.5)$ as shown in Fig. 9, and accounts for the periodicity of the domain in the x-direction. Vortices very far away have little effect on the computational domain so our initial data only accounts for the velocity prescribed by the vortices with $-500 \leq k \leq 500$. Each vortex is best expressed in polar coordinates with zero velocity in the radial direction and

$$V_\theta = \frac{1.5}{2\pi r}\left(1 - \exp\left(-\frac{r^2}{.5^2}\right)\right) \tag{42}$$

in the counterclockwise angular direction, where r is the distance from the vortex core. The initial velocity of the unreacted material is determined by summing the contribution from each of the 1001 vortices considered. See [20] for more details.

Figure 10 shows the time evolution of the flame front for a 140 by 280 grid cell computation illustrating how the counterclockwise vortices distort the flame front. The

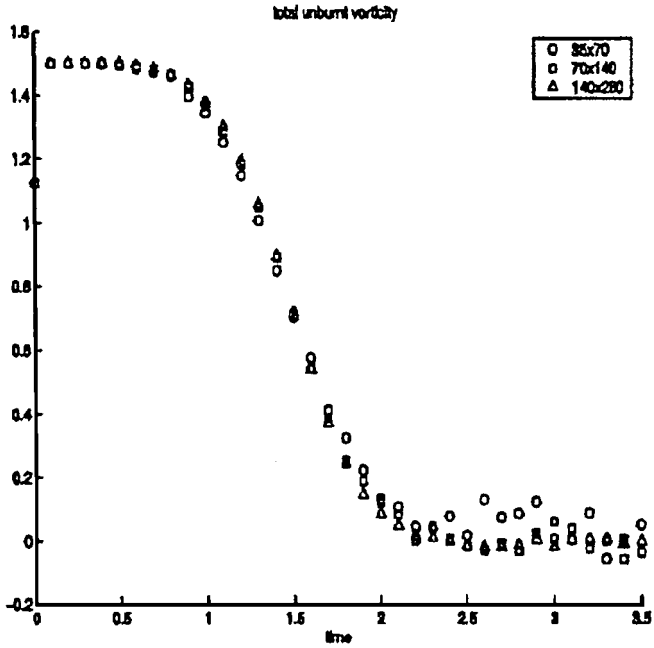

FIG. 18. Flame vortex interaction—total vorticity in the unburnt gas.

wrinkled wave travels along the flame front from left to right as the flame propagates through the array of vortices. Since the portion of the flame with positive slope is steeper than that with negative slope, the magnitude of the x-component of its flame speed is larger. Consequently, the intersection point between these two flame segments tends to move to

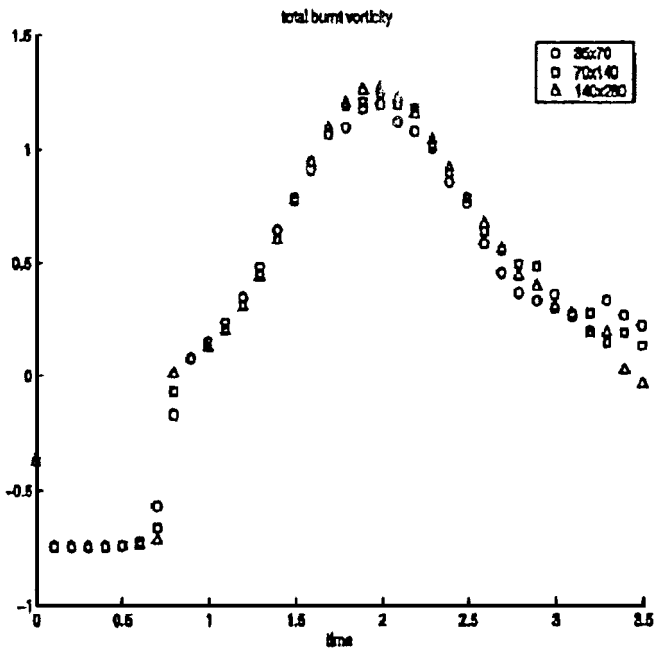

FIG. 19. Flame vortex interaction—total vorticity in the burnt gas.

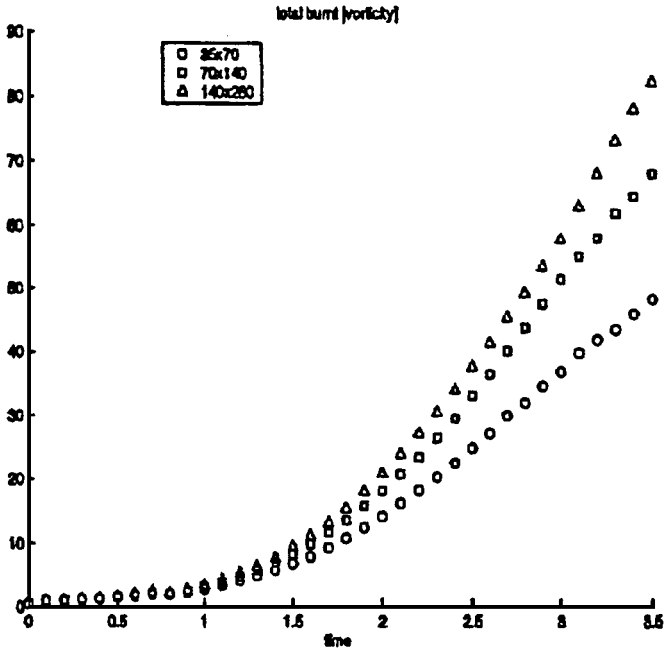

FIG. 20. Flame vortex interaction—total |vorticity| in the burnt gas.

the right. This traveling wave slows down later as the deformation becomes more symetrical. In Fig. 11, we show the results compared to those obtained after one level and two levels of grid coarsening. Note the first-order accurate convergence for the flame location.

As the flame moves downward and is distorted by the initial vortex, secondary vorticity is generated behind the flame front. Figure 12 shows the flame at $t = 1.5$ where part of the vortex has passed through the flame front and part of it can still be seen just below the flame. The secondary vorticity is positive on the right and left where the flame front has negative slope. Conversely, the secondary vorticity is negative in the center where the flame front has

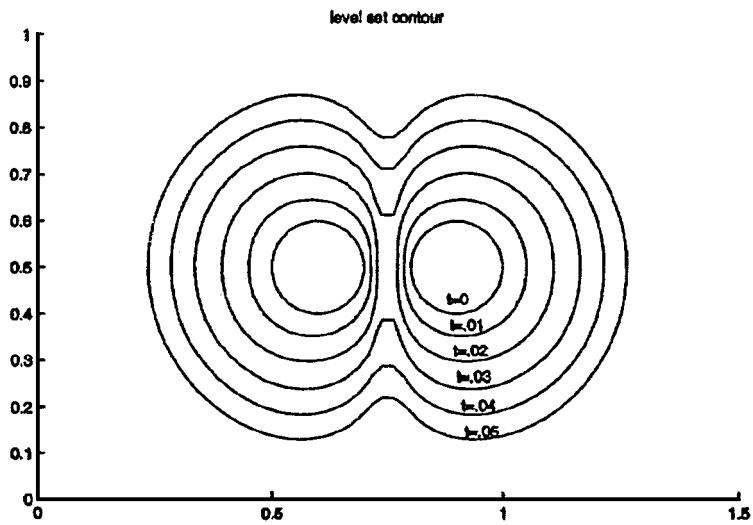

FIG. 21. Merging circular flames—time evolution of the flame location.

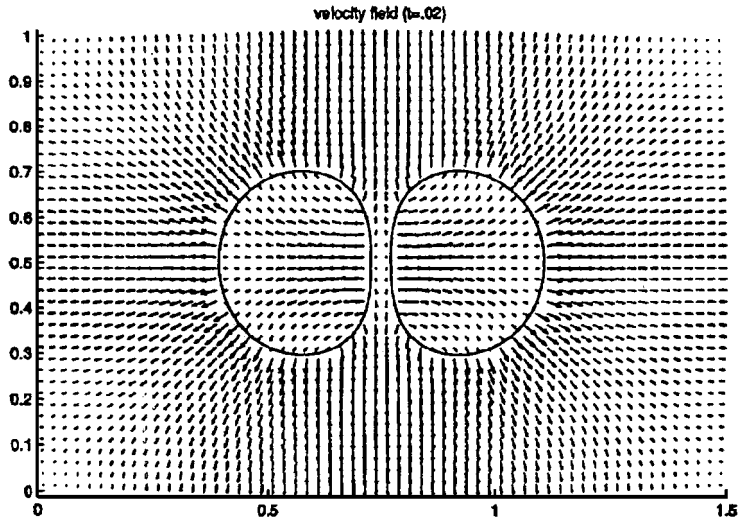

FIG. 22. Merging circular flames—velocity field before merging.

positive slope. In Fig. 11 at $t = 1$, the flame surface is perturbed with the disturbed middle segment having a positive slope. This orientation is due to the counterclockwise rotation of the vortex. This flame orientation subsequently generates a triple vorticity configuration with alternating signs on the burnt side of the flame characterized by positive vorticity behind the negatively sloped segments and negative vorticity behind the positively sloped segments. The highest vorticity is found to be at the flame tip where the flame front is most wrinkled. With further flame wrinkling, the magnitude of this flame-generated vorticity rapidly becomes higher than that of the initial vortex. Thus, as the flame propagates through the vortex, it continuously eliminates the initial radially symmetric vorticity substituting it with the triple vorticity configuration until the initial vortex core is totally wiped out at $t = 1.9$. Figure 13 shows the secondary vorticity at a later time of $t = 1.9$. To get some idea

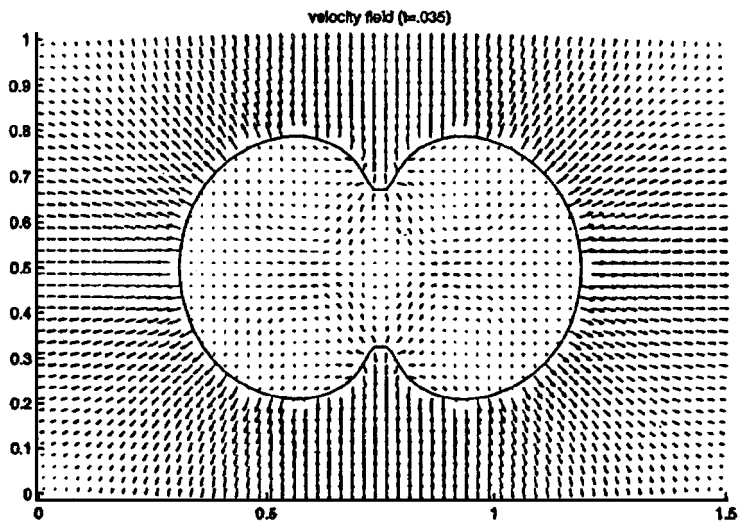

FIG. 23. Merging circular flames—velocity field after merging.

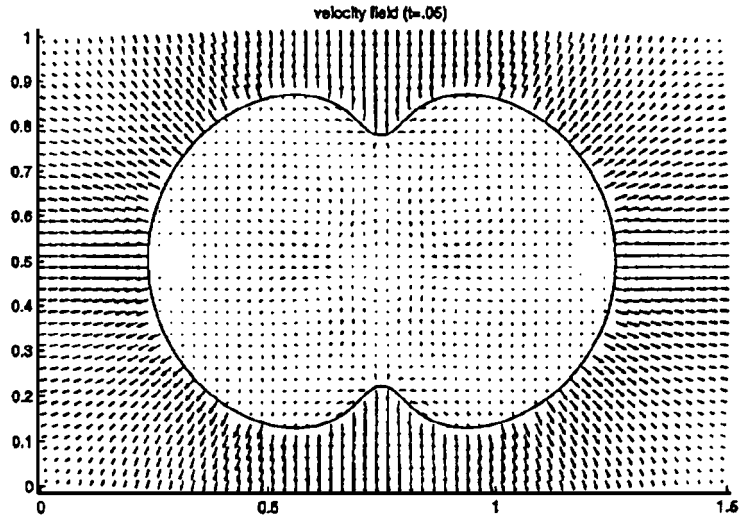

FIG. 24. Merging circular flames—velocity field later in time.

of how the vorticity behaves at different levels of grid resolution, Figs. 14 and 15 show the vorticity at $t = 1.9$ obtained with one level and two levels of grid refinement, respectively. Finally, Figs. 16 and 17 show the velocity fields at $t = 1.5$ and $t = 1.9$, respectively, for the coarsest 35×70 grid.

In order to see how the secondary vorticity generation proceeds in time, Figs. 18 and 19 show the total vorticity in the unreacted and reacted regions, respectively, as a function of time. Note that there is an initial startup error in the vorticity (and velocity) since the array of vortices are only initialized in the unburnt gas. This initial transient dies out quickly and could be avoided by initializing the vorticity in the burnt gas as well. Finally, since both

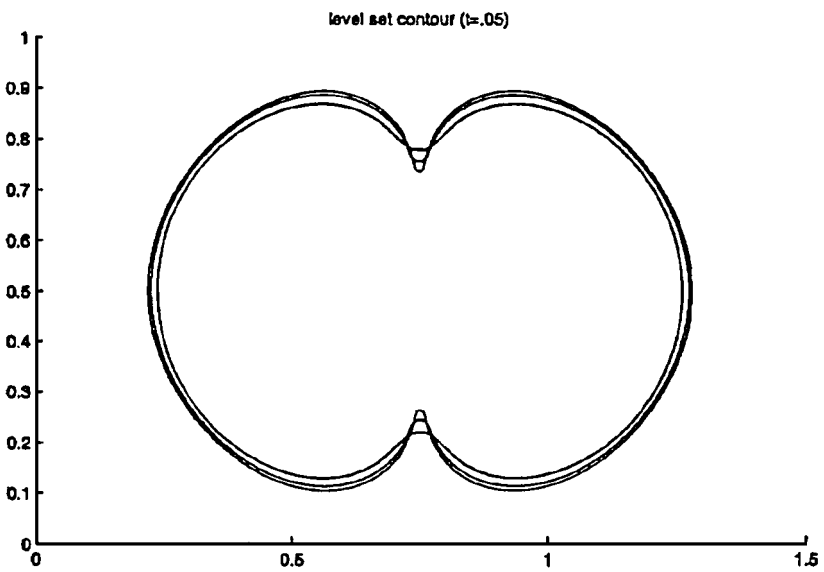

FIG. 25. Merging circular flames—grid refinement.

positive and negative vorticity increases the local turbulence, Fig. 20 shows the sum of the *magnitude* of vorticity in the reacted material as a function of time.

4.2.4. *Example 7*

Consider two circular flames centered at $(x, y) = (.6, .5)$ and $(x, y) = (.9, .5)$ both with radius $r = .1$ in a $[0, 1.5] \times [0, 1]$ domain with the reacted material inside the circles and the unreacted material outside the circles. The flame speed is given by $S = 1 + .01\kappa$, and Dirichlet, $p = 0$, boundary conditions were used on all sides of the domain. Figure 21 shows the time evolution of the flame front for a 60×40 grid cell computation. Figures 22, 23, and 24 show the velocity fields at different points in time. Note that the topological change (merging) requires no special treatment. Figure 25 shows the computation results for the 60×40 grid cell computation along with those obtained after one level and two levels of grid refinement. Note the first-order accurate convergence for the flame location.

4.3. Three Spatial Dimensions

4.3.1. *Example 8*

Consider two spherical flames centered at $(x, y, z) = (.6, .5, .5)$ and $(x, y, z) = (.9, .5, .5)$ both with radius $r = .1$ in a $[0, 1.5] \times [0, 1] \times [0, 1]$ domain with reacted material inside the spheres and unreacted material outside the spheres. The flame speed is given by $S = 1 + .01\kappa$, and Dirichlet, $p = 0$, boundary conditions were used on all sides of the domain. This is the three dimensional equivalent of Example 7. Figure 26 shows the evolution of the flame front in time for a $90 \times 60 \times 60$ grid cell calculation illustrating the ease of merging in three spatial dimensions.

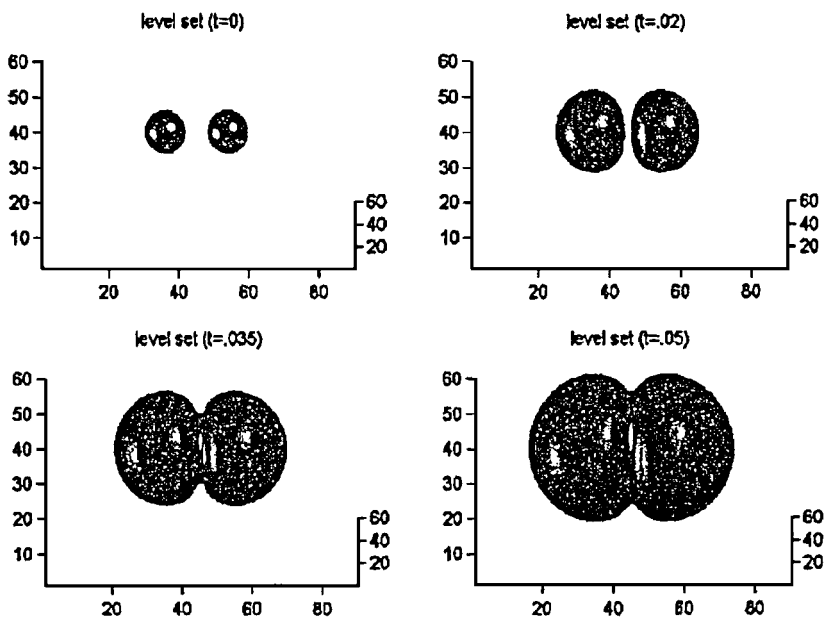

FIG. 26. Merging spherical flames.

5. CONCLUSION

A new simple numerical method based on the level set method and ghost fluid method was developed to simulate two-phase incompressible flow where one material is being converted into another. We presented this method in the context of premixed flame simulations. The flame was assumed to be a surface of discontinuity separating the reacted and unreacted gases, and propagating with a prescribed flame velocity. The incompressible Euler equations were solved on a stationary finite difference grid for both the reacted and the unreacted gases. The velocity and other material properties were modeled with jump discontinuities across the flame front where appropriate.

We demonstrated the accuracy and fidelity of the method by comparing the numerical results with exact solutions for a steady flame and the Darrieus–Landau instability. The robustness of the method was demonstrated by the simplicity with which flame fronts can merge. The method is fairly easily to implement and was extended to three spatial dimensions to treat a simple merging problem. Using this new numerical method, we studied the interaction of a flame and vortex with the objective of gaining further insight into the fundamental mechanisms governing flame generated vorticity resulting from baroclinic torque.

REFERENCES

1. J. U. Brackbill, D. B. Kothe, and C. Zemach, A continuum method for modeling surface tension, *J. Comput. Phys.* **100**, 335 (1992).
2. Y. C. Chang, T. Y. Hou, B. Merriman, and S. Osher, A level set formulation of Eulerian interface capturing methods for incompressible fluid flows, *J. Comput. Phys.* **124**, 449 (1996).
3. A. J. Chorin, numerical solution of the Navier–Stokes equations, *Math. Comp.* **22**, 745 (1968).
4. R. Fedkiw, T. Aslam, B. Merriman, and S. Osher, A non-oscillatory Eulerian approach to interfaces in multimaterial flows (the ghost fluid method), *J. Comput. Phys.* **152**, 457 (1999).
5. R. Fedkiw, T. Aslam, and S. Xu, The ghost fluid method for deflagration and detonation discontinuities, *J. Comput. Phys.* **154**, 393 (1999).
6. G. Golub and C. Van Loan, *Matrix Computations* (Johns Hopkins Press, Baltimore, 1989).
7. F. H. Harlow and J. E. Welch, Numerical calculation of time-dependent viscous incompressible flow of fluid with a free surface, *Phys. Fluids* **8**, 2182 (1965).
8. B. T. Helenbrook, personal communication.
9. B. T. Helenbrook, L. Martinelli, and C. K. Law, A numerical method for solving incompressible flow problems with a surface of discontinuity, *J. Comput. Phys.* **148**, 366 (1999).
10. B. T. Helenbrook and C. K. Law, The role of Landau–Darrieus instability in large scale flows, *Combustion Flame* **117**, 155 (1999).
11. D. Juric and G. Tryggvason, Computations of boiling flows, *Int. J. Multiphase Flow* **24**, 387 (1998).
12. M. Kang, R. Fedkiw, and X.-D Liu, A boundary condition capturing method for multiphase incompressible flow, *J. Sci. Comput.* **15**, 323 (2000).
13. X.-D. Liu, R. P. Fedkiw, and M. Kang, A boundary condition capturing method for Poisson's equation on irregular domains, *J. Comput. Phys.* **154**, 151 (2000).
14. G. H. Markstein, *Nonsteady Flame Propagation* (Pergamon, Oxford, 1964).
15. S. Osher and J. A. Sethian, Fronts propagating with curvature dependent speed: Algorithms based on Hamilton–Jacobi formulations, *J. Comput. Phys.* **79**, 12 (1988).
16. C. Peskin, Numerical analysis of blood flow in the heart, *J. Comput. Phys.* **25**, 220 (1977).
17. C. Peskin and B. Printz, Improved volume conservation in the computation of flows with immersed elastic boundaries, *J. Comput. Phys.* **105**, 33 (1993).
18. R. Peyret and T. D. Taylor, *Computational Methods for Fluid Flow* (Springer-Verlag, New York, 1983).

19. M. Sussman, P. Smereka, and S. Osher, A level set approach for computing solutions to incompressible two-phase flow, *J. Comput. Phys.* **114**, 146 (1994).
20. J. Qian, G. Tryggvason, and C. K. Law, A front method for the motion of premixed flames, *J. Comput. Phys.* **144**, 52 (1998).
21. C. W. Shu and S. Osher, Efficient implementation of essentially nonoscillatory shock capturing schemes, *J. Comput. Phys.* **77**, 439 (1988).
22. G. Son and V. K. Dir, Numerical simulation of film boiling near critical pressures with a level set method, *J. Heat Transfer* **120**, 183 (1998).
23. S. O. Unverdi and G. Tryggvason, A front-tracking method for viscous, incompressible, multi-fluid flows, *J. Comput. Phys.* **100**, 25 (1992).
24. S. Welch and J. Wilson, A volume of fluid based method for fluid flows with phase change, *J. Comput. Phys.* **160**, 662 (2000).
25. F. A. Williams, *The Mathematics of Combustion*, edited by J. D. Buckmaster Soc. for Industr. of Appl. Math., Philadelphia, 1985, pp. 97–131.